Photoionization microscopy in terms of local-frame-transformation theory

P. Giannakeas,* F. Robicheaux,† and Chris H. Greene‡
Department of Physics and Astronomy, Purdue University, West Lafayette, Indiana 47907, USA
(Received 16 October 2014; published 30 April 2015)

Two-photon ionization of an alkali-metal atom in the presence of a uniform electric field is investigated using a standardized form of the local-frame-transformation and generalized quantum defect theory. The relevant long-range quantum defect parameters in the combined Coulombic plus Stark potential are calculated with eigenchannel R-matrix theory applied in the downstream parabolic coordinate η. The present formulation permits us to express the corresponding microscopy observables through the local frame transformation, and it gives a critical test of the accuracy of the Harmin-Fano theory.

DOI: 10.1103/PhysRevA.91.043424 PACS number(s): 32.80.Fb, 32.60.+i, 07.81.+a

I. INTRODUCTION

The photoabsorption spectrum of an alkali-metal atom in the presence of a uniform electric field constitutes a fundamental testbed for atomic physics. Through the past few decades, study of this class of systems has provided key insights into their structure and chemical properties, and into the nonperturbative effect of an applied external field. The response of the lower-energy eigenstates of any alkali-metal atom to a laboratory strength electric field is perturbative and can be described in terms of the static atomic polarizability. For states high in the Rydberg series or in the ionization continuum, however, even a modest field strength nonperturbatively modifies the nature of the energy eigenstates.

In fact this problem touches on fundamental issues concerning the description of nonseparable quantum mechanical systems. The Stark effect of alkali-metal atoms is one of the simpler prototypes of such systems, because the short-distance electron motion is nearly separable in spherical coordinates while the intermediate- and long-distance motion is almost exactly separable in parabolic coordinates. The evolution of a quantum electron wave function from small to large distances thus involves a transformation, termed a *local* frame transformation (LFT) because it is derived in a localized region of space. (The extent of this region is typically limited to within 10–20 a.u. between the electron and the nucleus.)

When one encounters a problem of nonrelativistic quantum mechanics where the Schrödinger equation is nonseparable, one usually anticipates that the system will require a complicated numerical treatment. This is the first and most common approach even if the nonseparability is limited to only two coordinates as is the case with the nonhydrogenic Stark effect since the azimuthal angle ϕ is separable for this problem (aside from the comparatively weak spin-orbit coupling). Thus it was a major breakthrough when papers by Fano [1] and Harmin [2–4] showed in the early 1980s how the problem can be solved analytically and almost completely using ideas based on the frame transformation theory and quantum defect theory. Since that body of work introduced the LFT method, it has been generalized to other systems that are similar in having an intermediate region of space where the wave equation is separable in both the small- and large-distance coordinate systems. Example applications include diverse systems such as negative ion photodetachment in either an external magnetic [5] or electric field [6–9], and confinement-induced resonances in ultracold atom-atom scattering [10–13] or dipole-dipole collisions [14].

The LFT theory has been demonstrated by now to have great effectiveness in reproducing experimental spectra and collision properties as well as accurate theoretical results derived using other methods [15]. The deviations between highly accurate R-matrix calculations and the LFT method were found in Ref. [15] to be around 0.1% for resonance positions in the ^{7}Li Stark effect. The LFT is evolving as a general tool that can solve this class of nonseparable quantum mechanical problems, but it must be kept in mind that it is an approximate theory. It is therefore desirable to quantify the approximations made, in order to understand its regimes of applicability and where it is likely to fail.

The goal of the present study is to provide a critical assessment of the accuracy of the LFT, concentrating in particular on observables related to photoionization microscopy. The experiments in this field [16–19] have focused on the theoretical proposal that the probability distribution of an ejected slow continuum electron can be measured on a position-sensitive detector at a large distance from the nucleus [20–23].

While the Harmin-Fano LFT theory has been shown in the 1980s and 1990s to describe the total photoabsorption Stark spectra in one-electron [2,3,15] and two-electron [24–26] Rydberg states, examination of a differential observable such as the photodetachment [27] or photoionization [28] microscopy probability distribution should in principle yield a sharper test of the LFT. Indeed, a recent study (see Ref. [29]) identifies noticeable discrepancies between Harmin's LFT Stark effect theory and presumably more accurate coupled-channel calculations. Particularly in view of the extended applications of LFT theory to diverse physical contexts, such as the confinement-induced resonance systems noted above, a deeper understanding of the strengths and limitations of the LFT is desirable. On this basis and in view of the key findings of Ref. [29] a detailed discussion on its arguments is provided in Ref. [30].

In this paper we develop a fully quantal implementation of the Harmin local frame transformation, instead of relying on semiclassical wave mechanics as in Refs. [2–4]. The relevant

*pgiannak@purdue.edu
†robichf@purdue.edu
‡chgreene@purdue.edu

single-channel quantities in parabolic coordinates needed to implement the LFT theory are determined accurately using a variational R-matrix method. This allows us to disentangle errors associated with the WKB approximation from those deriving from the LFT approximation itself, as was shown in Ref. [15]. For the most part this causes only small differences from the original WKB treatment consistent with Ref. [15], but it is occasionally significant, for instance for the resonant states located very close to the top of the Stark barrier. Another goal of this study is to standardize the local frame transformation theory to fully specify the asymptotic form of the wave function which is needed to describe other observables such as the spatial distribution function (differential cross section) that is measured in photoionization microscopy.

We also revisit the interconnection between the irregular solutions from spherical to parabolic coordinates through the matching of the spherical and parabolic Green's functions in the small distance range where the electric field is far weaker than the Coulomb interaction. More specifically, a detailed analysis is focused on the matching of the principal value or smooth Green's functions in both coordinates at positive or negative energies, respectively. This allows us to quantitatively reexamine the way the irregular solutions are specified in the Fano-Harmin LFT, which is at the heart of the LFT method.

One of our major conclusions is that the LFT method does not exhibit large, qualitative inaccuracies for the photoionization microscopy of Na atoms ionized via a two-photon process in π polarized fields. We obtain excellent agreement between the approximate LFT theory and our virtually exact numerical calculations. Nevertheless some minor discrepancies are noted which may indicate minor inaccuracies of the local-frame-transformation theory. Specifically, our detailed tests do not confirm the problems with the LFT calculations claimed to have been identified by Ref. [29].

This paper is organized as follows. Section II focuses on the local-frame-transformation theory of the Stark effect and presents a general discussion of the physical content of the theory, including a description of the relevant mappings of the regular and irregular solutions of the Coulomb and Stark-Coulomb Schrödinger equation. Section III reformulates the local-frame-transformation theory properly, including a description of the asymptotic electron wave function. In addition, this section defines all of the relevant scattering observables. Section IV discusses a numerical implementation based on a two-surface implementation of the eigenchannel R-matrix theory. This toolkit permits us to perform accurate quantal calculations in terms of the local-frame-transformation theory, without relying on the semiclassical wave mechanics adopted in Harmin's implementation. Section V is devoted to a discussion of our recent finding in comparison with the conclusions of Ref. [29]. Finally, Sec. VI summarizes and concludes our analysis.

II. LOCAL-FRAME-TRANSFORMATION THEORY OF THE STARK EFFECT

This section reviews the local-frame-transformation theory (LFT) for the nonhydrogenic Stark effect, utilizing the same nomenclature introduced by Harmin [2–4]. The crucial parts of the corresponding theory are highlighted developing its standardized formulation.

A. General considerations

In the case of alkali-metal atoms at small length scales the impact of the alkali-metal ion core on the motion of the valence electron outside the core can be described effectively by a phase-shifted radial wave function:

$$\Psi_{\epsilon\ell m}(\mathbf{r}) = \frac{1}{r} Y_{\ell m}(\theta,\phi)[f_{\epsilon\ell}(r)\cos\delta_\ell - g_{\epsilon\ell}(r)\sin\delta_\ell], \quad r > r_0, \tag{1}$$

where the $Y_{\ell m}(\theta,\phi)$ are the spherical harmonic functions of orbital angular momentum ℓ and projection m. r_0 indicates the effective radius of the core; δ_ℓ denotes the phase that the electron acquires due to the alkali-metal ion core. These phases are associated with the quantum defect parameters, μ_ℓ, according to the relation $\delta_\ell = \pi\mu_\ell$. The pair of $\{f,g\}$ wave functions designate the regular and irregular Coulomb ones respectively whose Wronskian is $W[f,g] = 2/\pi$. We remark that this effective radius r_0 is placed close to the origin where the Coulomb field prevails over the external electric field. Therefore, the effect on the phases δ_ℓ from the external field can be neglected for typical laboratory field strengths. Note that atomic units are employed everywhere; otherwise is explicitly stated. In addition, we assume $m \geqslant 0$.

At distances $r \gg r_0$ the outermost electron of the nonhydrogenic atom is in the presence of a homogeneous static electric field oriented in the z direction. The separability of the center of mass and relative degrees of freedom permits us to describe all the relevant physics by the following Schrödinger equation in the relative frame of reference:

$$\left(-\frac{1}{2}\nabla^2 - \frac{1}{r} + Fz - \epsilon\right)\psi(\mathbf{r}) = 0, \tag{2}$$

where F indicates the strength of the electric field, r corresponds to the electron distance from the nucleus, and ϵ is the total colliding energy. Note that Eq. (2) is invariant under rotations around the polarization axis, whereby the corresponding azimuthal quantum number m is conserved to the extent that spin-orbit and hyperfine couplings can be neglected, as is done here. In contrast, the total orbital angular momentum is not conserved, which shows up as a coupling among different ℓ states. The latter challenge, however, can be circumvented by employing a coordinate transformation which results in a fully separable Schrödinger equation. Hence, in parabolic coordinates $\xi = r + z$, $\eta = r - z$, and $\phi = \tan^{-1}(x/y)$, Eq. (2) reads

$$\frac{d^2}{d\xi^2}\Xi^{\epsilon F}_{\beta m}(\xi) + \left(\frac{\epsilon}{2} + \frac{1-m^2}{4\xi^2} + \frac{\beta}{\xi} - \frac{F}{4}\xi\right)\Xi^{\epsilon F}_{\beta m}(\xi) = 0, \tag{3}$$

$$\frac{d^2}{d\eta^2}\Upsilon^{\epsilon F}_{\beta m}(\eta) + \left(\frac{\epsilon}{2} + \frac{1-m^2}{4\eta^2} + \frac{1-\beta}{\eta} + \frac{F}{4}\eta\right)\Upsilon^{\epsilon F}_{\beta m}(\eta) = 0, \tag{4}$$

where β is the *effective charge* and ϵ, F are the energy and the field strength in atomic units. We remark that Eq. (3) in the ξ degrees of freedom describes the bounded motion of the

electron since as $\xi \to \infty$ the electric potential energy steadily increases. This means that the Ξ wave function vanishes as $\xi \to \infty$ for every energy ϵ at particular quantized values of the effective charge β. Thus Eq. (3) can be regarded as a generalized eigenvalue equation where for each quantized $\beta \equiv \beta_{n_1}$ the $\Xi^{\epsilon F}_{\beta m} \equiv \Xi^{\epsilon F}_{n_1 m}$ wave function possesses n_1 nodes. In this case the wave functions $\Xi^{\epsilon F}_{n_1 m}(\xi)$ possess the following properties.

(i) Near the origin $\Xi^{\epsilon F}_{n_1 m}$ behaves as $\Xi^{\epsilon F}_{n_1 m}(\xi \to 0) \sim N^F_\xi \xi^{\frac{m+1}{2}}[1 + O(\xi)]$, where N^F_ξ is an energy-field-dependent amplitude and must be determined numerically in general.

(ii) The wave function $\Xi^{\epsilon F}_{n_1 m}$ obeys the following normalization condition: $\int_0^\infty \frac{[\Xi^{\epsilon F}_{n_1 m}(\xi)]^2}{\xi} d\xi = 1$.

On the other hand, Eq. (4) describes solely the motion of the electron in the η degree of freedom which is unbounded. As $\eta \to \infty$ the electric potential energy steadily decreases, which in combination with the Coulomb potential forms a barrier that often has a local maximum. Hence, for specific values of energy, field strength, and effective charge the corresponding wave function $\Upsilon^{\epsilon F}_{\beta m} \equiv \Upsilon^{\epsilon F}_{n_1 m}$ propagates either above or below the barrier local maximum where the states n_1 define asymptotic channels for the scattering wave function in the η degrees of freedom. Note that, for $\beta_{n_1} > 1$, the Coulomb term in Eq. (4) becomes repulsive and therefore no barrier formation occurs. Since Eq. (4) is associated with the unbounded motion of the electron it possesses two solutions, namely the solution $\Upsilon^{\epsilon F}_{n_1 m}(\eta)$ regular at $\eta = 0$ and an irregular one $\bar{\Upsilon}^{\epsilon F}_{n_1 m}(\eta)$ which can be chosen according to various criteria. This set of solutions has the following properties.

(i) Close to the origin and before the barrier the irregular solutions $\bar{\Upsilon}^{\epsilon F}_{n_1 m}(\eta)$ lag by $\pi/2$ the regular ones, denoted as $\Upsilon^{\epsilon F}_{n_1 m}(\eta)$. Note that their normalization follows Harmin's definition [2] and is clarified below.

(ii) Near the origin the regular solutions vanish according to the relation $\Upsilon^{\epsilon F}_{n_1 m}(\eta \to 0) \sim N^F_\eta \eta^{\frac{m+1}{2}}[1 + O(\eta)]$, where N^F_η is an energy- and field-dependent amplitude and must be determined numerically in general.

Next consider the behavior of the pair solutions $\{\Upsilon^{\epsilon F}_{n_1 m}, \bar{\Upsilon}^{\epsilon F}_{n_1 m}\}$ at distances past the barrier. Indeed, the regular and irregular functions can be written in the following WKB form:

$$\Upsilon^{\epsilon F}_{n_1 m}(\eta \gg \eta_0) \to \sqrt{\frac{2}{\pi k(\eta)}} \sin\left[\int_{\eta_0}^{\eta} k(\eta')d\eta' + \frac{\pi}{4} + \delta_{n_1}\right], \tag{5}$$

$$\bar{\Upsilon}^{\epsilon F}_{n_1 m}(\eta \gg \eta_0) \to \sqrt{\frac{2}{\pi k(\eta)}} \sin\left[\int_{\eta_0}^{\eta} k(\eta')d\eta' + \frac{\pi}{4} + \delta_{n_1} - \gamma_{n_1}\right], \tag{6}$$

where $k(\eta) = \sqrt{-m^2/\eta^2 + (1 - \beta_{n_1})/\eta + \epsilon/2 + F\eta/4}$ is the local momentum term with the Langer correction being included, η_0 is the position of the outermost classical turning point, and the phase δ_{n_1} is the absolute phase induced by the combined Coulomb and electric fields. The phase γ_{n_1} corresponds to the relative phase between the regular and irregular functions, namely $\{\Upsilon, \bar{\Upsilon}\}$. At short distances their relative phase is exactly $\pi/2$, though as they probe the barrier at larger distances their relative phase is altered and hence past the barrier the *short-range* regular and irregular functions differ by $0 < \gamma_{n_1} < \pi$ and not just $\pi/2$. We should remark that after the barrier the amplitudes of the pair $\{\Upsilon, \bar{\Upsilon}\}$ are equal to each other and their relative phase in general differs from $\pi/2$. On the other hand, at shorter distances before the barrier the amplitudes of the $\{\Upsilon, \bar{\Upsilon}\}$ basically are not equal to each other and their relative phase is exactly $\pi/2$. This yields that the Wronskian of the corresponding solutions possesses the same value at all distances and provides us with insight into the interconnection between amplitudes and relative phases.

The key concept of Harmin's theoretical framework is to translate the relevant spherical coordinate phases at short distances in the absence of an external field, i.e., δ_ℓ [see Eq. (1)] into the scattering amplitudes and phases at large distances in parabolic coordinates where the electric-field contributions cannot be neglected. This can be achieved by mapping the corresponding regular and irregular solutions from spherical to parabolic-cylindrical coordinates as we discuss in the following.

B. Mapping of the regular functions from spherical to parabolic-cylindrical coordinates

The most intuitive aspect embedded in the present problem is that the electron Hamiltonian right outside the core possesses a spherical symmetry which at greater distances due to the field becomes parabolic-cylindrically symmetric. Therefore, a proper coordinate transformation of the corresponding *energy normalized* wave functions from spherical to parabolic cylindrical coordinates will permit us to *propagate* to asymptotic distances the relevant scattering or photoionization events initiated near the core. Indeed at distances $r \ll F^{-1/2}$ the regular functions in spherical coordinates are related to the parabolic cylindrical ones according to the following relation:

$$\begin{aligned}\psi^{\epsilon F}_{n_1 m}(\mathbf{r}) &= \frac{e^{im\phi}}{\sqrt{2\pi}} \frac{\Xi^{\epsilon F}_{n_1 m}(\xi)}{\sqrt{\xi}} \frac{\Upsilon^{\epsilon F}_{n_1 m}(\eta)}{\sqrt{\eta}} \\ &= \sum_\ell U^{\epsilon F m}_{n_1 \ell} \frac{f_{\epsilon \ell m}(\mathbf{r})}{r} \quad \text{for } r \ll F^{-1/2},\end{aligned} \tag{7}$$

where $f_{\epsilon \ell m}(\mathbf{r})$ are the regular solutions in spherical coordinates with ℓ being the orbital angular momentum quantum number. The small distance behavior is $f_{\epsilon \ell m}(\mathbf{r}) \approx N_{\epsilon \ell} Y_{\ell m}(\theta, \phi) r^{\ell+1}[1 + O(r)]$ with $N_{\epsilon \ell}$ a normalization constant [see Eq. (13) in Ref. [2]]. Therefore, from the behavior at small distances of the parabolic-cylindrical and spherical solutions the frame transformation $U^{\epsilon F m}_{n_1 \ell}$ has the following form:

$$\begin{aligned}U^{\epsilon F m}_{n_1 \ell} = &\frac{N^F_\xi N^F_\eta}{N_{\epsilon \ell}} \frac{(-1)^m \sqrt{4\ell + 2} m!^2}{(2\ell + 1)!! \sqrt{(\ell + m)!(\ell - m)!}} \\ &\times \sum_k^{\ell - m} (-1)^k \binom{\ell - m}{k} \binom{\ell + m}{\ell - k} \\ &\times \frac{\nu^{m-\ell} \Gamma(n_1 + 1) \Gamma(\nu - n_1 - m)}{\Gamma(n_1 + 1 - k) \Gamma(\nu - n_1 + k - \ell)},\end{aligned} \tag{8}$$

where $n_1 = \beta_{n_1} \nu - 1/2 - m/2$ and $\nu = 1/\sqrt{-2\epsilon}$.

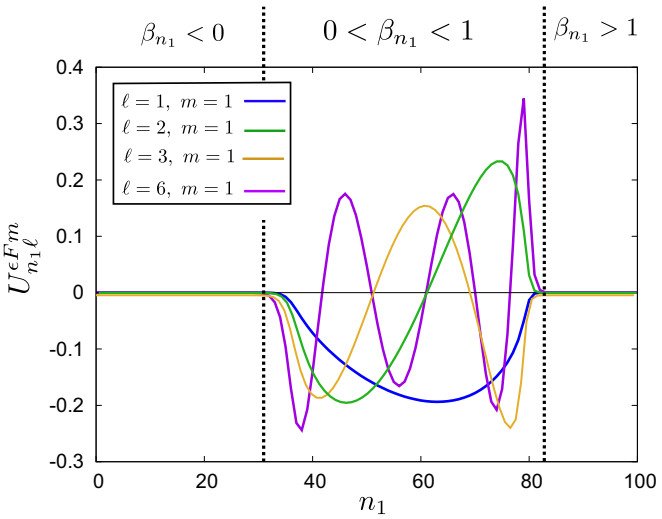

FIG. 1. (Color online) Matrix elements of the local frame transformation $U^{\epsilon Fm}_{n_1\ell}$ vs the number of states n_1 for $m = 1$ where the angular momentum acquires the values $\ell = 1$, 2, 3, and 6. The electric-field strength is $F = 640$ V/cm and total collisional energy is $\epsilon = 135.8231$ cm^{-1}. The vertical dashed lines indicate the sign and the interval of values of the β_{n_1}.

Figure 1 plots some elements of the local frame transformation matrix $\underline{U}$ in Eq. (8) as functions of the quantum number n_1, where again the integers n_1 label the eigenvalues β_{n_1}. The elements of the local-frame-transformation matrix $\underline{U}$ are plotted for four different angular momenta, namely $\ell = 1$, 2, 3, and 6 where we set $m = 1$ at energy $\epsilon = 135.8231$ cm^{-1} and field $F = 640$ V/cm. One sees that the matrix elements of $\underline{U}$ become significant in the interval $n_1 \in (38,79)$ which essentially corresponds to $\beta_{n_1} \in (0,1)$. For $\beta_{n_1} < 0$ or $\beta_{n_1} > 1$ the local frame transformation vanishes rapidly. This behavior mainly arises from the normalization amplitudes N^F_ξ and N^F_η, which obey the following relations:

$$N^F_\xi \sim \frac{\beta_{n_1}}{1 - e^{-2\pi\beta_{n_1}/k}}, \quad N^F_\eta \sim \frac{(1-\beta_{n_1})}{1 - e^{-2\pi(1-\beta_{n_1})/k}}. \tag{9}$$

Note that these expressions are approximately valid only for positive energies and they are exact for $F = 0$.

From the expressions in Eq. (9) it becomes evident that for negative eigenvalues β_{n_1} the amplitude N^F_ξ vanishes exponentially while N^F_η remains practically finite. Similarly, for the case of $\beta_{n_1} > 1$ the amplitude N^F_η vanishes exponentially, and these result in the behavior depicted in Fig. 1. Another aspect of the elements of the local-frame-transformation matrix $\underline{U}$ are their nodal pattern shown in Fig. 1. For increasing ℓ the corresponding number of nodes increases as well. For $m = 1$, every $U^{\epsilon Fm}_{n_1\ell}$ possesses $\ell - 1$ nodes.

Figure 2 shows the LFT matrix elements at the same field strength but negative energies, i.e., $\epsilon = -135.8231$ cm^{-1}, whereas the azimuthal quantum number is set to be $m = 1$. Unlike the case of positive energies which is demonstrated in Fig. 1, at negative energies the presence of the Stark barrier dominates, and controls the amplitudes of the regular function in the η coordinate. This mainly arises due to the fact that the corresponding function for high n_1 states tunnels

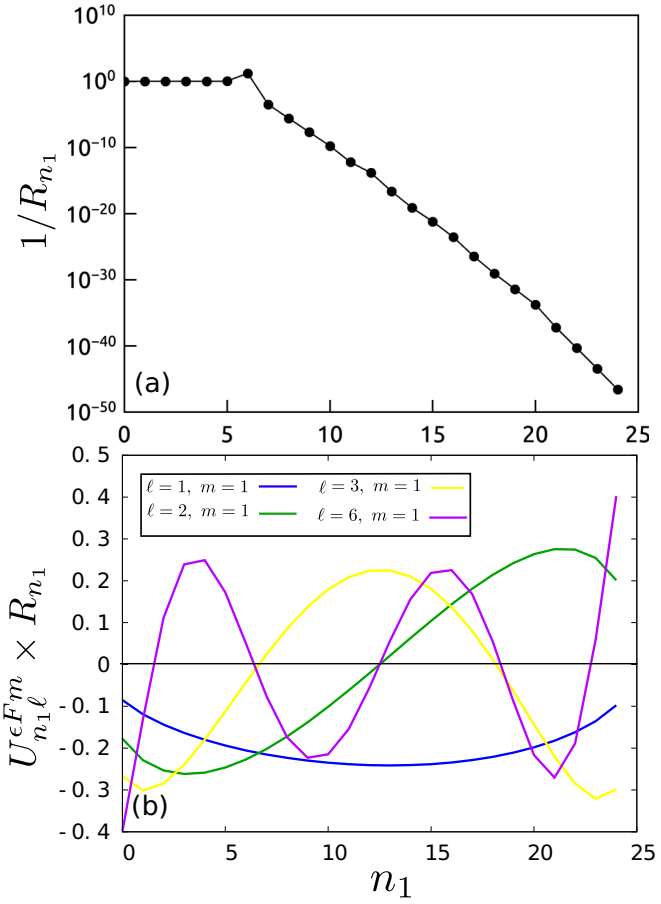

FIG. 2. (Color online) (a) Amplitudes $1/R_{n_1}$ and (b) the matrix elements $U^{\epsilon Fm}_{n_1\ell} R_{n_1}$ as a function of the number of states n_1 for $m = 1$. In panel (b) the angular momentum acquires the values $\ell = 1$, 2, 3, and 6 indicated by the blue, green, yellow, and purple solid lines, respectively. The electric-field strength is $F = 640$ V/cm and total energy is $\epsilon = -135.8231$ cm^{-1}.

under the Stark barrier. Therefore, away from Stark resonances these short-range amplitudes become strongly suppressed. In order to view these effects one can factor the amplitude N^F_η according to the relation $N^F_\eta = N^{F=0}_\eta (1/R_{n_1})$, where the term $N^{F=0}_\eta$ is the amplitude that does not explicitly depend on the Stark field, whereas the term $1/R_{n_1}$ is the amplitude that fully encapsulates the impact of the barrier. Figure 2(a) illustrates the dependence of the amplitude $1/R_{n_1}$ as a function of the n_1 states, where we observe that as n_1 increases the width of the Stark barrier increases yielding a vanishing amplitude $1/R_{n_1}$. In panel (b) of Fig. 2 the LFT matrix elements are depicted where the strong dependence on the barrier is absorbed by multiplying them with the amplitudes R_{n_1}. This permits us to observe features similar to the case of positive energies. Namely in Fig. 2(b) the matrix elements $U^{\epsilon Fm}_{n_1\ell} R_{n_1}$ behave as the associated Legendre polynomials exhibiting $\ell - 1$ nodes for $m = 1$. In addition, the considered interval of n_1 states corresponds to effective charges $\beta_{n_1} < 1$ as in Fig. 1. However, unlike the case of positive energies, the values $\beta_{n_1} > 1$ are not depicted due to the fact the regular functions of the η coordinate become imaginary and therefore the LFT matrix elements will acquire imaginary values.

C. Mapping of the irregular functions from spherical to parabolic-cylindrical coordinates

Having established the mapping between the regular solutions of the wave function in spherical and parabolic-cylindrical coordinates, the following focuses on the relation between the irregular ones.

The irregular solution in parabolic-cylindrical coordinates has the following form:

$$\chi^{\epsilon F}_{n_1 m}(\mathbf{r}) = \frac{e^{im\phi}}{\sqrt{2\pi}} \frac{\Xi^{\epsilon F}_{n_1 m}(\xi)}{\sqrt{\xi}} \frac{\bar{\Upsilon}^{\epsilon F}_{n_1 m}(\eta)}{\sqrt{\eta}}, \tag{10}$$

Recall that in order to relate Eq. (10) to the irregular functions in spherical coordinates we employ Green's functions as was initially suggested in Ref. [1]. In the following, we consider two cases with respect to positive and negative energies and firmly address the proper matching of a specific Green's function of the pure Coulomb Hamiltonian with a Green's function of Coulomb plus Stark Hamiltonian.

For positive energies the outgoing Green's function of the pure Coulomb Hamiltonian, namely $G^{(C,\mathrm{out})}(\mathbf{r},\mathbf{r}')$, in spherical coordinates is written as follows:

$$G^{(C,\mathrm{out})}(\mathbf{r},\mathbf{r}') = G^{(C)}_P(\mathbf{r},\mathbf{r}') + \frac{i\pi}{rr'} \sum_{\ell} f_{\epsilon\ell m}(\mathbf{r}) f_{\epsilon\ell m}(\mathbf{r}'), \tag{11}$$

where the first term is the principal value Green's function, whereas the second term fulfills the homogeneous Schrödinger equation. The functions f correspond to the regular functions as they are defined in Eq. (1).

Equation (11) is uniquely defined by obeying proper boundary conditions at the origin and at infinity. However, in multichannel quantum defect theory one might drop the latter boundary condition and focus on the principal Green's function. The principal value Green's function consists of a sum of products of regular and irregular functions with their relative phase being exactly $\pi/2$ [31,32] which, expressed in spherical coordinates, reads

$$G^{(C)}_P(\mathbf{r},\mathbf{r}') = \frac{\pi}{rr'} \sum_{\ell,m} f_{\epsilon\ell m}(\mathbf{r}) g_{\epsilon\ell m}(\mathbf{r}'), \quad r < r', \tag{12}$$

where the $\{f,g\}$ solutions correspond to the regular and irregular functions as they are defined in Eq. (1).

In general, the principal value Green's function of the Coulomb Hamiltonian in spherical and in parabolic-cylindrical coordinates are equal to each other, namely $G^{(C),\mathrm{sc}}_P \equiv G^{(C),\mathrm{pcc}}_P$ (the abbreviations sc and pcc stand for spherical and parabolic-cylindrical coordinates, respectively). In return the parabolic coordinate principal value Green's function for the pure Coulomb Hamiltonian $G^{(C,\mathrm{pcc})}_P(\mathbf{r},\mathbf{r}')$ is matched with a Green's function of the Coulomb plus Stark Hamiltonian $G^{(C+F)}(\mathbf{r},\mathbf{r}')$, which is also expressed in parabolic-cylindrical coordinates. Of course, in general the two Green's functions differ from each other since they correspond to different Schrödinger equations. However, at small distances the field term in the Stark Hamiltonian becomes negligible in comparison with the Coulomb term. Therefore, in this restricted region of the configuration space, i.e., $r \ll F^{-1/2}$, the Stark Hamiltonian is virtually identical to the Coulomb Hamiltonian. Following this prescription allows one to interconnect the irregular functions of both coordinate systems at positive energies. A similar procedure can be employed for negative energies as well.

More specifically for negative energies, by analytically continuing the $\{f,g\}$ Coulombic functions across the threshold yields the relation $\mathcal{G}^{(C),\mathrm{sc}} \equiv \mathcal{G}^{(C),\mathrm{pcc}}$. The $\mathcal{G}^{(C)}$ is the so-called *smooth* Green's function, which is related to a Green's function bounded at $r = 0$ and at infinity according to the expression [33]

$$G^{(C)}(\mathbf{r},\mathbf{r}') = \mathcal{G}^{(C)}(\mathbf{r},\mathbf{r}') + \frac{\pi}{rr'} \sum_{\ell} f_{\epsilon\ell m}(\mathbf{r}) \cot\beta(\epsilon) f_{\epsilon\ell m}(\mathbf{r}'), \tag{13}$$

where $\beta(\epsilon) = \pi(\nu - \ell)$ with $\nu = 1/\sqrt{-2\epsilon}$ is the phase accumulated from $r = 0$ up to $r \to \infty$. Assume that ϵ_n (i.e., $\nu \to n \in \aleph^*$) are the eigenenergies specified by imposing the boundary condition at infinity where n denotes a counting index of the corresponding bound states. Then in the right-hand side of Eq. (13) the second term at energies $\epsilon = \epsilon_n$ diverges while the first term is free of poles. The smooth Green's function is identified as the one where the two linearly independent solutions have their relative phase equal to $\pi/2$ *at small distances*. Furthermore, the singularities in Eq. (13) originate from imposing the boundary condition at infinity, though in the spirit of multichannel quantum defect theory we can drop this consideration and solely employ the $\mathcal{G}^{(C)}$ which in spherical coordinates reads

$$\mathcal{G}^{(C)}(\mathbf{r},\mathbf{r}') = \frac{\pi}{rr'} \sum_{\ell,m} f_{\epsilon\ell m}(\mathbf{r}) g_{\epsilon\ell m}(\mathbf{r}'), \quad r < r' \quad \text{for } \epsilon < 0. \tag{14}$$

In view of the now established equality between the principal value (smooth) Green's functions at positive (negative) energies in spherical and parabolic cylindrical coordinates for the pure Coulomb Hamiltonian, the discussion can proceed to the Stark Hamiltonian. Hence as mentioned above in the Coulomb zone, i.e., $r \ll F^{-1/2}$, the Stark Hamiltonian is approximately equal to the pure Coulomb one. This implies the existence of a Green's function, $G^{(C+F)}$, for the Stark Hamiltonian which is equal to the $G^{(C),\mathrm{pcc}}_P$ ($\mathcal{G}^{(C),\mathrm{pcc}}$), and which in turn is equal to Eq. (12) [Eq. (14)] at positive (negative) energies. More specifically, the $G^{(C+F)}$ Green's function expressed in parabolic-cylindrical coordinates is given by the expression

$$G^{(C+F)}(\mathbf{r},\mathbf{r}') = 2 \sum_{n_1,m} \frac{\psi^{\epsilon F}_{n_1 m}(\mathbf{r}) \chi^{\epsilon F}_{n_1 m}(\mathbf{r}')}{W\left(\Upsilon^{\epsilon F}_{n_1 m}, \bar{\Upsilon}^{\epsilon F}_{n_1 m}\right)} \quad \text{for } \eta < \eta' \ll F^{-1/2}, \tag{15}$$

where the functions $\{\psi,\chi\}$ are the regular and irregular solutions of the Stark Hamiltonian, which at small distances (in the classically allowed region) have a relative phase of $\pi/2$. This originates from $\pi/2$ relative phase of the $\{\Upsilon,\bar{\Upsilon}\}$ as was mentioned is subsection A. The Wronskian $W[\Upsilon^{\epsilon F}_{n_1 m}, \bar{\Upsilon}^{\epsilon F}_{n_1 m}] = (2/\pi)\sin\gamma_{n_1}$ yields $\{\psi,\chi\}$ solutions have the same energy normalization as in the $\{f,g\}$ Coulomb functions.

From the equality between Eqs. (12) [or (14)] and (15), hereafter with the additional use of Eq. (7), the mapping of the

irregular solutions is given by the following expression:

$$\frac{g_{\epsilon\ell m}(\mathbf{r})}{r} = \sum_{n_1} \chi^{\epsilon F}_{n_1 m}(\mathbf{r}) \csc\left(\gamma_{n_1}\right)(\underline{U})^{\epsilon Fm}_{n_1\ell} \quad \text{for } r \ll F^{-1/2}. \tag{16}$$

Additionally, Eq. (7) conventionally can be written as

$$\frac{f_{\epsilon\ell m}(\mathbf{r})}{r} = \sum_{n_1} \psi^{\epsilon F}_{n_1 m}(\mathbf{r})[(\underline{U}^T)^{-1}]^{\epsilon Fm}_{n_1\ell} \quad \text{for } r \ll F^{-1/2}. \tag{17}$$

Note that in Eqs. (16) and (17) $\underline{U}^T$ and $[\underline{U}^T]^{-1}$ are the transpose and inverse transpose matrices of the $\underline{U}$ LFT matrix whose elements are given by $(\underline{U})^{\epsilon Fm}_{n_1\ell} = U^{\epsilon Fm}_{n_1\ell}$.

In Ref. [15] Stevens *et al.* comment that in Eq. (16) only the left-hand side possesses a uniform shift over the θ angles. Quantifying this argument, one can examine the difference of the semiclassical phases with and without the electric field. Indeed, for a zero-energy electron the phase accumulation due to the existence of the electric field as a function of the angle θ obeys the expression

$$\begin{aligned}\Delta\phi(r,\theta) &= \int^r k(r,\theta)dr - \int^r k_0(r)dr \\ &\approx -\frac{\sqrt{2}}{5} F r^{5/2}\cos\theta \quad \text{for } Fr^2 \ll 1,\end{aligned} \tag{18}$$

where $k(r,\theta)$ $[k_0(r)]$ indicates the local momentum with (without) the electric field F. In Eq. (18) it is observed that for field strength $F = 1$ kV/cm and $r < 50$ a.u. the phase modification due to existence of the electric field is less than 0.001 radians. This simply means that at short distances both sides of Eq. (16) should exhibit practically uniform phase over the angle θ.

Recapitulating Eqs. (16) and (17) constitute the mapping of the irregular and regular functions respectively from spherical to parabolic cylindrical coordinates, respectively.

III. SCATTERING OBSERVABLES IN TERMS OF THE LOCAL FRAME TRANSFORMATION

This section implements the Harmin frame-transformation theory to determine the relevant scattering observables.

A. Asymptotic form of the frame-transformed irregular solution and the reaction matrix

The irregular solutions which we defined in Eq. (6) are not the *usual* ones of the scattering theory since in the asymptotic region, namely $\eta \to \infty$, they do not lag by $\pi/2$ the regular functions, Eq. (5). Hence this particular set of irregular solutions should not be used in order to obtain the scattering observables which are properly defined in the asymptotic region.

However, by linearly combining Eqs. (5) and (6) we define a new set of irregular solutions which are energy-normalized, asymptotically lag by $\pi/2$ the regular ones, and read

$$\bar{\Upsilon}^{\epsilon F,\mathrm{scat}}_{n_1 m}(\eta) = \frac{1}{\sin\gamma_{n_1}} \bar{\Upsilon}^{\epsilon F}_{n_1 m}(\eta) - \cot\gamma_{n_1}\Upsilon^{\epsilon F}_{n_1 m}(\eta), \tag{19}$$

where this equation together with Eq. (5) correspond to a set of real irregular and regular solutions according to the usual conventions of scattering theory.

The derivation of the reaction matrix follows. Equations (19) and (10) are combined and then substituted into Eq. (16) such that the irregular solution in spherical coordinates is expressed in terms of the $\bar{\Upsilon}^{\epsilon F,\mathrm{scat}}_{n_1 m}$:

$$\frac{g_{\epsilon\ell m}(\mathbf{r})}{r} = \sum_{n_1}\left[\psi^{\epsilon F}_{n_1 m}(\mathbf{r})\cot\left(\gamma_{n_1}\right) + \chi^{\epsilon F,\mathrm{scat}}_{n_1 m}(\mathbf{r})\right](\underline{U}^T)^{\epsilon Fm}_{\ell n_1}, \tag{20}$$

where $\chi^{\epsilon F,\mathrm{scat}}_{n_1 m}(\mathbf{r})$ is defined as

$$\chi^{\epsilon F,\mathrm{scat}}_{n_1 m}(\mathbf{r}) = e^{im\phi}\,\Xi^{\epsilon F}_{n_1 m}(\xi)\bar{\Upsilon}^{\epsilon F,\mathrm{scat}}_{n_1 m}(\eta)/\sqrt{2\pi\xi\eta}. \tag{21}$$

Hereafter, the short-range wave function [Eq. (1)] expressed in spherical coordinates is transformed via the LFT matrix $\underline{U}$ into the asymptotic wave function. Specifically,

$$\begin{aligned}\Psi_{\epsilon\ell m}(\mathbf{r}) = \sum_{n_1} \psi^{\epsilon F}_{n_1 m}(\mathbf{r})\big[&[(\underline{U}^T)^{-1}]^{\epsilon Fm}_{n_1\ell}\cos\delta_\ell \\ &- \cot\gamma_{n_1}(\underline{U})^{\epsilon Fm}_{n_1\ell}\sin\delta_\ell\big] - \chi^{\epsilon F}_{n_1 m}(\mathbf{r})(\underline{U})^{\epsilon Fm}_{n_1\ell}\sin\delta_\ell.\end{aligned} \tag{22}$$

Then from Eq. (22) and after some algebraic manipulations the reaction matrix solutions are written in a compact matrix notation as

$$\begin{aligned}\mathbf{\Phi}^{(R)}(\mathbf{r}) &= \mathbf{\Psi}[\cos\underline{\delta}]^{-1}\underline{U}^T[\underline{I} - \cot\underline{\gamma}\,\underline{U}\,\tan\underline{\delta}\underline{U}^T]^{-1} \\ &= \bar{\psi}(\mathbf{r}) - \bar{\chi}(\mathbf{r})[\underline{U}\,\tan\underline{\delta}\underline{U}^T][\underline{I} - \cot\underline{\gamma}\,\underline{U}\,\tan\underline{\delta}\underline{U}^T]^{-1},\end{aligned} \tag{23}$$

where $\underline{I}$ is the identity matrix, the matrices $\cos\underline{\delta}$, $\tan\underline{\delta}$, and $\cot\underline{\gamma}$ are diagonal ones. Note that $\bar{\psi}$ $(\bar{\chi})$ indicates a vector whose elements are the $\psi^{\epsilon F}_{n_1 m}(\mathbf{r})$ $[\chi^{\epsilon F}_{n_1 m}(\mathbf{r})]$ functions. Similarly, the elements of the vector $\mathbf{\Psi}$ are provided by Eq. (1). Then from Eq. (24) the reaction matrix obeys the following relation:

$$\underline{R} = \underline{U}\,\tan\underline{\delta}\underline{U}^T[\underline{I} - \cot\underline{\gamma}\,\underline{U}\,\tan\underline{\delta}\underline{U}^T]^{-1}. \tag{24}$$

In fact the matrix product $\underline{U}\,\tan\underline{\delta}\underline{U}^T$ can be viewed as a reaction matrix $\underline{\mathcal{K}}$ which does not yet encapsulate the impact of the Stark barrier on the wave function. Moreover, as shown in Ref. [34] the recasting of the expression for the reaction matrix $\underline{R}$ into a form that does not involve the inverse $[\underline{U}^T]^{-1}$ improves its numerically stability. In addition, it can be shown with simple algebraic manipulations that the reaction matrix is symmetric. Note that this reaction matrix $\underline{R}$ should not be confused with the Wigner-Eisenbud R matrix.

The corresponding *physical* S matrix is defined from the R matrix via a Cayley transformation, namely

$$\begin{aligned}\underline{S} &= [\underline{I} + i\underline{R}][\underline{I} - i\underline{R}]^{-1} \\ &= [\underline{I} - (\cot\underline{\gamma} - i\underline{I})\underline{\mathcal{K}}][\underline{I} - (\cot\underline{\gamma} + i\underline{I})\underline{\mathcal{K}}]^{-1},\end{aligned} \tag{25}$$

where clearly this S matrix is equivalent to the corresponding result of Ref. [29]. Also, the S matrix in Eq. (25) is unitary since the corresponding R matrix is real and symmetric.

B. Dipole matrix and outgoing wave function with the atom-radiation field interaction

As was already discussed, the pair of parabolic regular and irregular solutions $\{\psi,\chi\}$ are the standing-wave solutions of the corresponding Schrödinger equation. However, by linearly

combining them and using Eq. (24), the corresponding energy-normalized outgoing-incoming wave functions are expressed as

$$\tilde{\mathbf{\Psi}}^{\pm}(\mathbf{r}) = \mp\mathbf{\Phi}_R(\mathbf{r})[\underline{I} \mp i\underline{R}]^{-1} = \frac{\mathbf{X}^{\mp}(\mathbf{r})}{i\sqrt{2}} - \frac{\mathbf{X}^{\pm}(\mathbf{r})}{i\sqrt{2}}[\underline{I} \pm i\underline{R}][\underline{I} \mp i\underline{R}]^{-1}, \quad (26)$$

where the elements of the vectors $\mathbf{X}^{\pm}(\mathbf{r})$ are defined by the relation $[\mathbf{X}^{\pm}(\mathbf{r})]^{\epsilon F}_{n_1 m} = [-\chi^{\epsilon F}_{n_1 m}(\mathbf{r}) \pm i\psi^{\epsilon F}_{n_1 m}(\mathbf{r})]/\sqrt{2}$.

In the treatment of the photoionization of alkali-metal atoms, the dipole matrix elements are needed to compute the cross sections which characterize the excitation of the atoms by photon absorption. Therefore, initially we assume that at small distances the short-range dipole matrix elements possess the form $d_\ell = \langle \Psi_{\epsilon\ell m}|\,\hat{\varepsilon}\cdot\hat{r}\,|\Psi_{\rm init}\rangle$. Note that the term $\hat{\varepsilon}\cdot\hat{r}$ is the dipole operator, the $\hat{\varepsilon}$ denotes the polarization vector, and $|\Psi_{\rm init}\rangle$ indicates the initial state of the atom. Then the dipole matrix elements which describe the transition amplitudes from the initial to each n_1th of the reaction-matrix states is

$$D^{(R)}_{n_1} = \sum_{\ell} d_\ell \{[\cos\underline{\delta}]^{-1}\underline{U}^T[\underline{I} - \cot\underline{\gamma}\,\underline{K}]^{-1}\}_{\ell n_1}. \quad (27)$$

Now with the help of Eq. (27) we define the dipole matrix elements for transitions from the initial state to the incoming wave final state which has only outgoing waves in the n_1th channel. The resulting expression is

$$D^{(-)}_{n_1} = \sum_{n_1'} D^{(R)}_{n_1'}[(\underline{I} - i\underline{R})^{-1}]_{n_1' n_1}. \quad (28)$$

Equation (28) provides the necessary means to properly define the outgoing wave function with the atom-field radiation. As it was shown in Ref. [35] the outgoing wave function can be derived as a solution of an inhomogeneous Schrödinger equation that describes the atom being perturbed by the radiation field. Formally this implies that

$$[\epsilon - H]\Psi_{\rm out}(\mathbf{r}) = \hat{\varepsilon}\cdot\hat{r}\Psi_{\rm init}(\mathbf{r}), \quad (29)$$

where $\Psi_{\rm out}(\mathbf{r})$ describes the motion of the electron after its photoionization moving in the presence of an electric field; H is the Stark Hamiltonian with ϵ being the energy of ionized electron. The $\Psi_{\rm out}(\mathbf{r})$ can be expanded in outgoing wave functions involving the dipole matrix elements of Eq. (28). More specifically, we have that

$$\Psi_{\rm out}(\mathbf{r}) = \sum_{n_1 m} D^{(-)}_{n_1 m} X^{\epsilon F,+}_{n_1 m}(\mathbf{r}). \quad (30)$$

C. Wave-function microscopy and differential cross sections

Recent experimental advances [16–19] have managed to detect the square modulus of the electronic wave function, which complements a number of corresponding theoretical proposals [20–23]. This has been achieved by using a position-sensitive detector to measure the flux of slow electrons that are ionized in the presence of an electric field.

The following defines the relevant observables associated with the photoionization microscopy. The key quantity is the differential cross section which in turn is defined through the electron current density. As in Ref. [35], consider a detector placed beneath the atomic source with its plane being perpendicular to the horizontal axis of the electric field. Then, with the help of Eq. (30) the electron current density in cylindrical coordinates has the following form:

$$R(\rho, z_{\rm det}, \phi) = \frac{2\pi\omega}{c}{\rm Im}\left[-\Psi_{\rm out}(\mathbf{r})^*\frac{d}{dz}\Psi_{\rm out}(\mathbf{r})\right]_{z=z_{\rm det}}, \quad (31)$$

where $z_{\rm det}$ indicates the position of the detector along the z axis, c is the speed of light, and ω denotes the frequency of the photon being absorbed by the electron. The integration of the azimuthal ϕ angle leads to the differential cross section per unit length in the ρ coordinate. Namely, we have that

$$\frac{d\sigma(\rho, z_{\rm det})}{d\rho} = \int_0^{2\pi} d\phi\,\rho\,R(\rho, z_{\rm det}, \phi). \quad (32)$$

IV. ONE-DIMENSIONAL EIGENCHANNEL R-MATRIX CALCULATION

Harmin's Stark effect theory for nonhydrogenic atoms is mainly based on the semiclassical WKB approach. In order to eliminate the WKB approximation as a potential source of error, this section implements a fully quantal description of Harmin's theory based on a variational eigenchannel R-matrix calculation as was formulated in Refs. [36,37] and reviewed in Ref. [38]. As implemented here using a B-spline basis set, the technique also shares some similarities with the Lagrange-mesh R-matrix formulation developed by Baye and co-workers [39]. The present application to a 1D system with both an inner and an outer reaction surface accurately determines regular and irregular solutions of the Schrödinger equation in the η degrees of freedom. The present implementation can be used to derive two independent solutions of any one-dimensional Schrödinger equation of the form

$$\left[-\frac{1}{2}\frac{d^2}{d\eta^2} + V(\eta)\right]\psi(\eta) = \frac{1}{4}\epsilon\psi(\eta), \quad (33)$$

where

$$V(\eta) = \frac{m^2-1}{8\eta^2} - \frac{1-\beta}{2\eta} - \frac{F}{8}\eta. \quad (34)$$

The present application of the noniterative eigenchannel R-matrix theory adopts a reaction surface Σ with two disconnected parts, one at an inner radius η_1 and the other at an outer radius η_2. The reaction volume Ω is the region $\eta_1 < \eta < \eta_2$.

This one-dimensional R-matrix calculation is based on the previously derived variational principle [36,40] for the eigenvalues b of the R-matrix,

$$b[\psi] = \frac{\int_\Omega[-\vec{\nabla}\psi^*\cdot\vec{\nabla}\psi + 2\psi^*(E-V)\psi]d\Omega}{\int_\Sigma \psi^*\psi\,d\Sigma}. \quad (35)$$

Physically, these R-matrix eigenstates have the same outward normal logarithmic derivative everywhere on the reaction surface, which consists here of these two points Σ_1 and Σ_2. The desired eigenstates obey the following boundary condition:

$$\frac{\partial\psi}{\partial n} + b\psi = 0 \quad \text{on } \Sigma. \quad (36)$$

In the present application the ψ-wave functions are expanded as a linear combination of a nonorthogonal B-spline basis [41], i.e.,

$$\psi(\eta) = \sum_i P_i B_i(\eta) = \sum_C P_C B_C(\eta) + P_I B_I(\eta) + P_O B_O(\eta), \tag{37}$$

where P_i denote the unknown expansion coefficients and $B_i(\eta)$ stands for the B-spline basis functions. The first term in the left-hand side of Eq. (37) was regarded as the "closed-type" basis set in Ref. [38] because every function $B_c(\eta)$ vanishes on the reaction surface, i.e., $B_c(\eta_1) = B_c(\eta_2) = 0$. The two basis functions $B_I(\eta)$ and $B_O(\eta)$ correspond to the "open-type" basis functions of Ref. [38] in that they are the only B-spline functions that are nonzero on the reaction surface. Specifically, only $B_I(\eta)$ is nonzero on the inner surface $\eta = \eta_1$ (Σ_1) and only $B_O(\eta)$ is nonzero on the outer surface $\eta = \eta_2$ (Σ_2). Moreover, the basis functions B_I and B_O have no region of overlap in the matrix elements discussed below.

Insertion of this trial function into the variational principle leads to the following generalized eigenvalue equation:

$$\underline{\Gamma} P = b \underline{\Lambda} P. \tag{38}$$

In addition, the real, symmetric matrices $\underline{\Gamma}$ and $\underline{\Lambda}$ are given by the following expressions for this one-dimensional problem:

$$\Gamma_{ij} = \int_{\eta_1}^{\eta_2} \left[\left(\frac{1}{2}\epsilon - 2V(\eta) \right) B_i(\eta) B_j(\eta) - B_i'(\eta) B_j'(\eta) \right] d\eta, \tag{39}$$

$$\Lambda_{ij} = B_i(\eta_1) B_j(\eta_1) + B_i(\eta_2) B_j(\eta_2) = \delta_{i,I}\delta_{I,j} + \delta_{i,O}\delta_{O,j}, \tag{40}$$

where δ indicates the Kronecker symbol and the $'$ are regarded as the derivatives with respect to the η.

It is convenient to write this linear system of equations in a partitioned matrix notation, namely,

$$\underline{\Gamma}_{CC} P_C + \underline{\Gamma}_{CI} P_I + \underline{\Gamma}_{CO} P_O = 0, \tag{41}$$

$$\underline{\Gamma}_{IC} P_C + \underline{\Gamma}_{II} P_I = b P_I, \tag{42}$$

$$\underline{\Gamma}_{OC} P_C + \underline{\Gamma}_{OO} P_O = b P_O. \tag{43}$$

Now the first of these three equations is employed to eliminate P_C by writing it as $P_C = -\underline{\Gamma}_{CC}^{-1}\underline{\Gamma}_{CI} P_I - \underline{\Gamma}_{CC}^{-1}\underline{\Gamma}_{CO} P_O$, which is equivalent to the "streamlined transformation" in Ref. [37]. This gives finally a 2×2 matrix $\underline{\Omega}$ to diagonalize at each ϵ in order to find the two R-matrix eigenvalues b_λ and corresponding eigenvectors $P_{i\lambda}$:

$$\begin{pmatrix} \underline{\Omega}_{II} & \underline{\Omega}_{IO} \\ \underline{\Omega}_{OI} & \underline{\Omega}_{OO} \end{pmatrix} \begin{pmatrix} P_I \\ P_O \end{pmatrix} = b \begin{pmatrix} P_I \\ P_O \end{pmatrix}. \tag{44}$$

Here, e.g., the matrix element $\underline{\Omega}_{II} \equiv \underline{\Gamma}_{II} - \underline{\Gamma}_{IC}\underline{\Gamma}_{CC}^{-1}\underline{\Gamma}_{CI}$, etc.

In any 1D problem like the present one, the use of a B-spline basis set leads to a banded structure for $\underline{\Gamma}_{CC}$ which makes the construction of $\underline{\Gamma}_{CC}^{-1}\underline{\Gamma}_{CI}$ and $\underline{\Gamma}_{CC}^{-1}\underline{\Gamma}_{CO}$ highly efficient in terms of memory and computer processing time; this step is the slowest in this method of solving the differential equation, but still manageable even in complex problems where the dimension of $\underline{\Gamma}_{CC}$ can grow as large as 10^4 to 10^5.

Again, the indices C refer to the part of the basis expansion that is confined fully within the reaction volume and vanishes on both reaction surfaces.

The diagonalization of Eq. (44) provides us with the b_λ eigenvalues and the corresponding eigenvectors, which define two linearly independent wave functions ψ_λ, with $\lambda = 1,2$. These obey the Schrödinger equation, Eq. (33), and have equal normal logarithmic derivatives at η_1 and η_2. The final step is to construct two linearly independent solutions that coincide at small η with the regular and irregular field-free η solutions $f_{\epsilon\beta m}(\eta)$ and $g_{\epsilon\beta m}(\eta)$ (cf. the Appendix). These steps are rather straightforward and are not detailed further in this paper.

V. RESULTS AND DISCUSSION

A. Frame-transformed irregular solutions

In this subsection the convergence of the frame-transformed irregular solutions, namely Eq. (16), is investigated both at positive and negative energies. This permits us to analyze the validity of the matching of the principal value Green's functions or the smooth ones for positive or negative energies, respectively. In return, this allows us to investigate the claims by Zhao *et al.* [29], which suggest an error in the frame-transformed irregular functions of the Coulomb-Stark Hamiltonian.

Figure 3 illustrates the irregular solutions in spherical coordinates where $\mathbf{r} = (r, \theta = 5\pi/6, \phi = 0)$ and the azimuthal quantum number is set to be $m = 1$. The energy is taken to be $\epsilon = 135.8231$ cm^{-1} and the field strength is $F = 640$ V/cm. In addition we focus on the regime where $r < 90$ a.u. $\ll F^{-1/2}$. In all the panels the black solid line indicates the analytically known irregular Coulomb function, namely $\frac{g^{(C)}_{\epsilon\ell m}(\mathbf{r})}{r}$. Figures 3(a)–3(c) examine the cases of angular momentum $\ell = 1$ and 6, respectively. All the green dashed lines, the diamonds, and dots correspond to the frame-transformed irregular Coulomb functions in spherical coordinates, namely $\frac{g^{(\mathrm{LFT})}_{\epsilon\ell m}(\mathbf{r})}{r}$, which are calculated by summing up from zero to n_1 the irregular $\chi^{\epsilon F}_{n_1 m}(\mathbf{r})$ functions in the parabolic coordinates as Eq. (16) indicates.

The positive value of the energy ensures that all the n_1 channels lie well above the local maximum in η whereby the phase parameter γ_{n_1} is very close to its semiclassical expected value $\pi/2$. Furthermore, since only short distances are relevant to this comparison, namely $r < 90$ a.u., this means that the summed $\bar{\Upsilon}^{\epsilon F}_{n_1 m}(\eta)$ functions on the right-hand side of Eq. (16) in the n_1th irregular $\chi^{\epsilon F}_{n_1 m}(\mathbf{r})$ will be equal to analytically known Coulomb irregular functions in the parabolic coordinates. This is justified since at the interparticle distances that we are interested in, namely $\ll F^{-1/2}$, the electric field is negligible in comparison to the Coulomb interaction. Then the corresponding Schrödinger equation becomes equal to the Schrödinger equation of the pure Coulomb field, which is analytically solvable in spherical and parabolic coordinates as well. Thus, in the following, we employ the above-mentioned considerations in the evaluation of the right-hand side of Eq. (16) for Figs. 3 and 4.

Figure 3(a) compares the radial irregular Coulomb function (black line) with those calculated in the LFT theory for $\ell = m = 1$. In order to check the convergence of the LFT

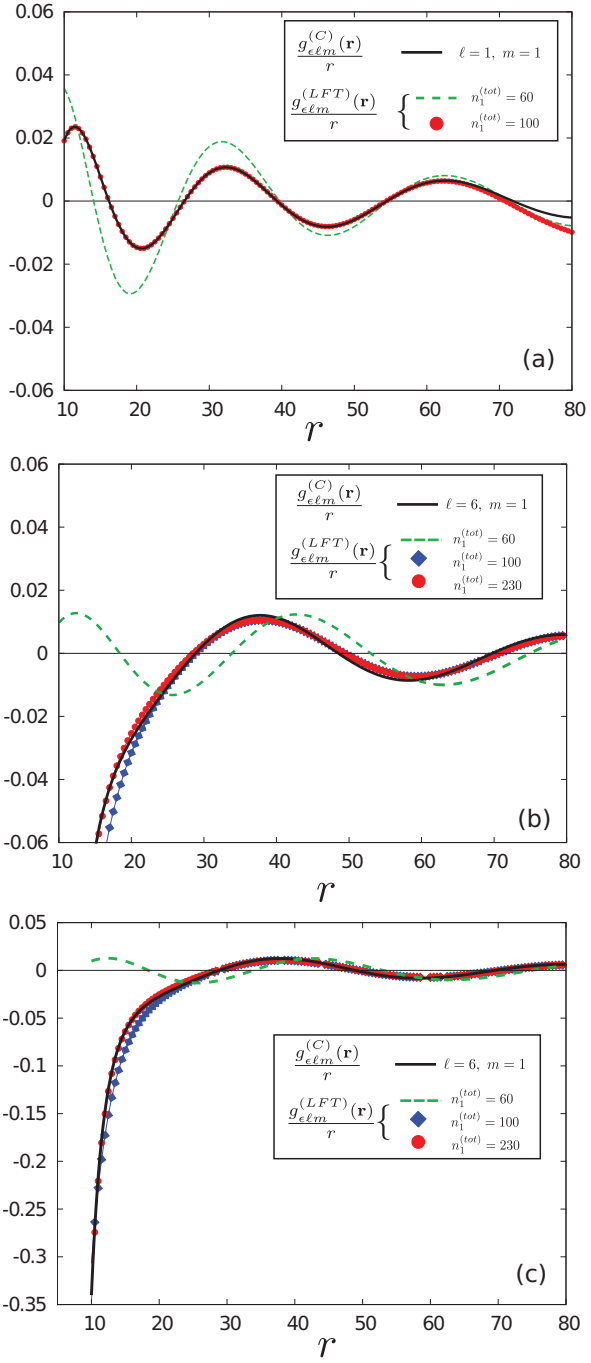

FIG. 3. (Color online) Irregular solutions in spherical coordinates illustrated up to $r = 80$ a.u. where $\mathbf{r} = (r,\theta = 5\pi/6,\phi = 0)$. In all panels the azimuthal quantum number is set to $m = 1$ and the black solid line indicates the irregular Coulomb function in spherical coordinates, namely $\frac{g^{(C)}_{\epsilon\ell m}(\mathbf{r})}{r}$. Panel (a) depicts the case of $\ell = 1$ where $\frac{g^{(\mathrm{LFT})}_{\epsilon\ell m}(\mathbf{r})}{r}$ denotes the irregular function in spherical coordinates calculated within the local-frame-transformation (LFT) framework, for two different cases of the total amount of n_1 states, namely $n_1^{(\mathrm{tot})} = 60$ (green dashed line) and $n_1^{(\mathrm{tot})} = 100$ (red dots). Panel (b) refers to the case of $\ell = 6$ where $\frac{g^{(\mathrm{LFT})}_{\epsilon\ell m}(\mathbf{r})}{r}$ is calculated for $n_1^{(\mathrm{tot})} = 60$ (green dashed line), $n_1^{(\mathrm{tot})} = 100$ (blue diamonds), and $n_1^{(\mathrm{tot})} = 230$ (red dots) states. Note that panel (c) is a zoomed-out plot of the curves shown in panel (b). In all panels the energy is $\epsilon = 135.8231$ cm^{-1} and the field is $F = 640$ V/cm.

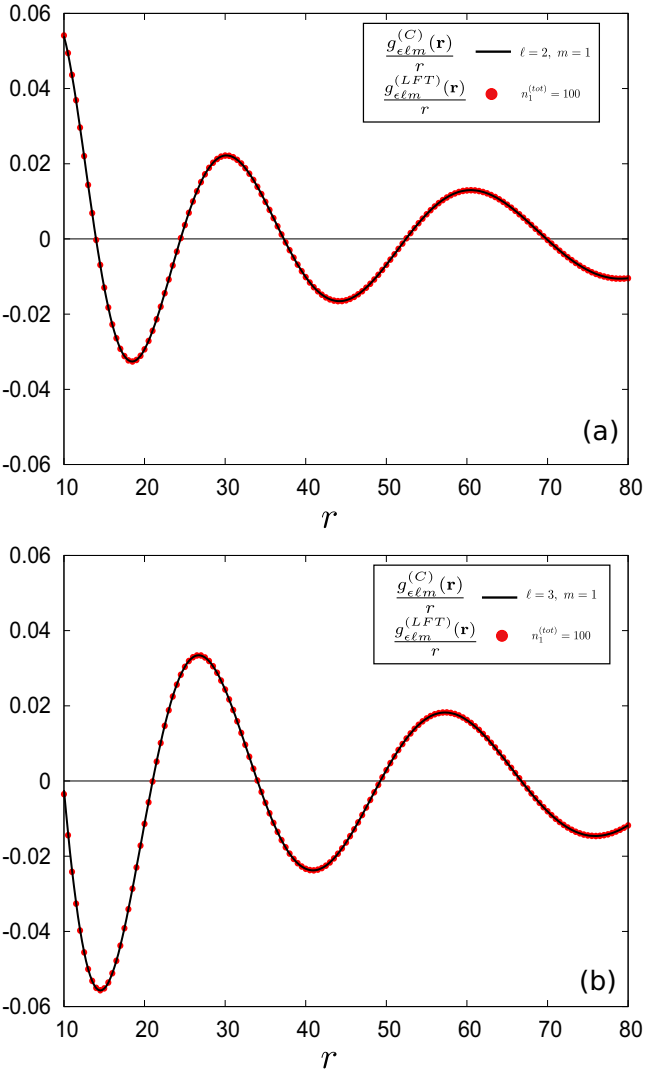

FIG. 4. (Color online) Irregular solutions in spherical coordinates are shown up to $r = 80$ a.u. where $\mathbf{r} = (r,\theta = 5\pi/6,\phi = 0)$. In all panels the azimuthal quantum number is set to be $m = 1$ and the black solid line indicates the analytically known irregular Coulomb function, namely $\frac{g^{(C)}_{\epsilon\ell m}(\mathbf{r})}{r}$. Panel (a) depicts the case of $\ell = 2$ where $\frac{g^{(\mathrm{LFT})}_{\epsilon\ell m}(\mathbf{r})}{r}$ denotes the irregular function in spherical coordinates calculated within the local-frame-transformation (LFT) framework for $n_1^{(\mathrm{tot})} = 100$ states (red dots). Similarly, panel (b) refers to the case of $\ell = 3$ with $\frac{g^{(C)}_{\epsilon\ell m}(\mathbf{r})}{r}$ being calculated for $n_1^{(\mathrm{tot})} = 100$ (red dots) states. In all panels the energy is $\epsilon = 135.8231$ cm^{-1} and the field is $F = 640$ V/cm.

calculations with respect to the total number $n_1^{(\mathrm{tot})}$ different values are considered. Indeed, we observe that the $\frac{g^{(\mathrm{LFT})}_{\epsilon\ell m}(\mathbf{r})}{r}$ for $n_1^{(\mathrm{tot})} = 60$ (green dashed line) does not coincide with $\frac{g^{(C)}_{\epsilon\ell m}(\mathbf{r})}{r}$ (black line) particularly in the interval of small interparticle distances r. This can be explained with the help of Fig. 1, which demonstrates that the LFT matrix $\underline{U}$ for $\ell = 1$ possesses nonzero elements for $n_1 > 60$, and those elements are crucial for the growth of the irregular solution at small distances. Therefore, the summation in Eq. (16) for $\ell = 1$ does not

begin to achieve convergence until $n_1 \geqslant 100$, where the corresponding elements of the LFT matrix $\underline{U}$ tend to zero. Indeed, when the sum over n_1 states is extended to this larger range, the irregular function $\frac{g^{(\mathrm{LFT})}_{\epsilon\ell m}}{r}$ of LFT theory, i.e., for $n_1^{(\mathrm{tot})} = 100$ (red dots), accurately matches the spherical field-free irregular solution $\frac{g^{(C)}_{\epsilon\ell m}(\mathbf{r})}{r}$ (black line) (see Fig. 3) at small electron distances r.

Furthermore, Fig. 3(b) refers to the case of $\ell = 6m = 1$. Specifically, for $n_1^{\mathrm{tot}} = 60$ states the $\frac{g^{(\mathrm{LFT})}_{\epsilon\ell m}}{r}$ (green dashed line) agrees poorly with the $\frac{g^{(C)}_{\epsilon\ell m}}{r}$ (black line). Though as in the case of $\ell = 1$, by increasing the number of n_1 states summed over in Eq. (16) the corresponding $\frac{g^{(\mathrm{LFT})}_{\epsilon\ell m}}{r}$, namely to $n_1^{(\mathrm{tot})} = 100$ (blue diamonds) and to $n_1^{(\mathrm{tot})} = 230$ (red dots), better agreement is achieved with the $\frac{g^{(C)}_{\epsilon\ell m}}{r}$. In contrast to the case where $\ell = 1$, the convergence is observed to be very slow for $\ell = 6$. The main reason for this is that for $r < 20$ a.u. we are in the classically forbidden region where $\frac{g^{(\mathrm{LFT})}_{\epsilon\ell m}}{r}$ diverges as $1/r^{\ell+1}$. From Eq. (16) it is clear that the sum will diverge due to the divergent behavior of the irregular functions of the η direction, namely the $\bar{\Upsilon}^{\epsilon F}_{n_1 m}(\eta)$. Hence, in order for the $\bar{\Upsilon}^{\epsilon F}_{n_1 m}(\eta)$ to be divergent in the interval of 10 to 80 a.u. it is important to take into account many n_1 states which correspond to $\beta_{n_1} > 1$ since only then the term $(1 - \beta_{n_1})/\eta$ becomes repulsive and producing the diverging behavior appropriate to a classical forbidden region. Figure 3(c) is a zoomed-out version of the functions shown in panel (b), which demonstrates that the $\frac{g^{(\mathrm{LFT})}_{\epsilon\ell m}}{r}$ for $n_1^{(\mathrm{tot})} = 230$ correctly captures the divergent behavior of $\frac{g^{(C)}_{\epsilon\ell m}}{r}$ for $r < 20$.

Similarly, Fig. 4 explores the cases of $\ell = 2$ [see Fig. 4(a)] and $\ell = 3$ [see Fig. 4(b)]. In both panels the black solid lines indicate the field-free Coulomb function in spherical coordinates $\frac{g^{(C)}_{\epsilon\ell m}}{r}$ and the red dots correspond to the $\frac{g^{(\mathrm{LFT})}_{\epsilon\ell m}}{r}$ for $n_1^{(\mathrm{tot})} = 100$. Both panels exhibit $\frac{g^{(\mathrm{LFT})}_{\epsilon\ell m}}{r}$ that are in excellent agreement with $\frac{g^{(C)}_{\epsilon\ell m}}{r}$.

Having analyzed the LFT calculations at positive energies, Fig. 5 illustrates the corresponding LFT calculations at negative energies, namely $\epsilon = -135.8231\ \mathrm{cm}^{-1}$ where the field strength is set to be $F = 640\ \mathrm{V/cm}$. In all panels the azimuthal quantum number is considered to be $m = 1$, the solid black lines denote the analytically known irregular Coulomb function $[\frac{g^{(C)}_{\epsilon\ell m}(\mathbf{r})}{r}]$, and red dots refer to the corresponding LFT calculations $[\frac{g^{(\mathrm{LFT})}_{\epsilon\ell m}(\mathbf{r})}{r}]$. In Figs. 5(a)–5(d) the $\ell = 1, 2, 3$, and 6 cases are considered at $\mathbf{r} = (r, \theta = \frac{5\pi}{6}, \phi = 0)$, respectively. In addition, for all the panels of Fig. 5 in the LFT calculations the summation over the n_1 states is truncated at $n_1^{\mathrm{tot}} = 25$ for the considered energy and field strength values. This simply means that the contributing terms in the summation of the frame-transformed irregular function correspond to fractional charges β_{n_1} less than unit. These states essentially describe all the relevant physics since only for these states the "down field" part of the wave function can probe the core either above or below the Stark barrier. Therefore, the n_1 states for which $\beta_{n_1} > 1$ physically are irrelevant since they yield a strongly repulsive barrier in the down field degree of freedom shielding completely the core. However, for these states the considered pair of regular and irregular functions in Sec. II C for the η degree of freedom acquire imaginary parts due to the fact that the colliding energy is below the minimum of the corresponding Coulomb potential. Consequently, these states are omitted from the sum of the frame-transformed irregular function. The omission of states with $\beta_{n_1} > 1$ mainly addresses the origin of the accuracy in the LFT calculations.

The impact of the omitted states is demonstrated in Fig. 5 where discrepancies are observed as the orbital angular momentum ℓ increases since more n_1 states are needed. Indeed, in panels (a)–(c) of Fig. 5 a good agreement is observed between the frame-transformed irregular function and the Coulombic one (black solid line). On the other hand, in panel (d) of Fig. 5 small discrepancies, particularly for $r > 20$, are observed occurring due to poor convergence over the summation of the n_1 states. However, these discrepancies are of minor importance since they correspond to negligible quantum defects, and thus yield minor contributions into the photoabsorption cross section.

The bottom line of the computations shown in this subsection is that the frame-transformed irregular Coulomb functions $\frac{g^{(\mathrm{LFT})}_{\epsilon\ell m}}{r}$ do not display, at least for $\ell = 1$ or 2, qualitative inaccuracies. For negative energies, our evidence suggests that the inclusion of n_1 states with $\beta_{n_1} > 1$ will enhance the accuracy of the frame-transformed irregular functions as was already demonstrated by the LFT calculations at positive energies.

B. Photoionization microscopy

Next we compute the photoionization microscopy observable for Na atoms, namely the differential cross section in terms of the LFT theory. The system considered is a two step photoionization of ground-state Na in the presence of an electric field F of strength 3590 V/cm. The two consecutive laser pulses are assumed to be π polarized along the field axis, which trigger in succession the following two transitions: (i) the excitation of the ground state to the intermediate state $^2P_{3/2}$, namely $[\mathrm{Ne}]3s\ ^2S_{1/2} \rightarrow [\mathrm{Ne}]3p\ ^2P_{3/2}$ and (ii) the ionization from the intermediate state $^2P_{3/2}$. In addition, due to spin-orbit coupling the intermediate state will be in a superposition of the states which are associated with different orbital azimuthal quantum numbers, i.e., $m = 0$ and 1. Hyperfine depolarization effects are neglected in the present calculations.

Figure 6 illustrates the differential cross section $\frac{d\sigma(\rho, z_{\mathrm{det}})}{d\rho}$ for Na atoms, where the detector is placed at $z_{\mathrm{det}} = -1$ mm and its plane is perpendicular to the direction of the electric field. Since spin-orbit coupling causes the photoelectron to possess both azimuthal orbital quantum numbers $m = 0, 1$, the contributions from both quantum numbers are explored in the following. Figure 6 panels (a) and (c) illustrate the partial differential cross section for transitions of $m_{\mathrm{int}} = 0 \rightarrow m_f = 0$, where m_{int} indicates the *intermediate* state azimuthal quantum number and m_f denotes the corresponding quantum number in the final state. Similarly, panels (b) and (d) in Fig. 6 are for the transitions $m_{\mathrm{int}} = 1 \rightarrow m_f = 1$. In addition, in all panels of Fig. 6 the red solid lines correspond to the LFT calculations, whereas the black dots indicate the *ab*

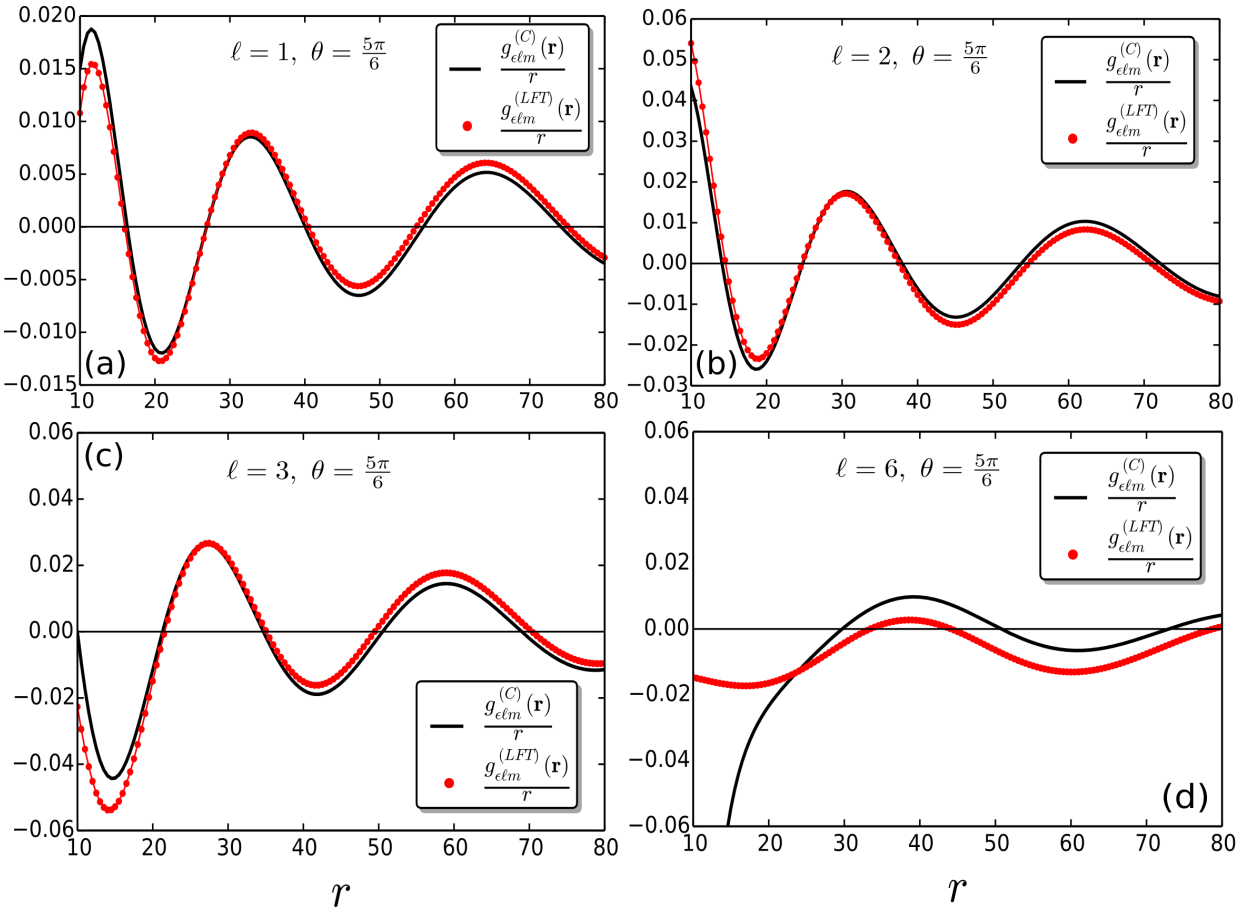

FIG. 5. (Color online) Irregular solutions in spherical coordinates at negative energies, i.e., $\epsilon = -135.8231\ \mathrm{cm}^{-1}$, illustrated for $\mathbf{r} = (r, \theta = \frac{5\pi}{6}, \phi = 0)$ with field $F = 640$ V/cm. In all panels the azimuthal quantum number is set to be $m = 1$ and the black solid line indicates the analytically known irregular Coulomb function, namely $\frac{g^{(C)}_{\epsilon\ell m}(\mathbf{r})}{r}$. Accordingly, the red dots correspond to the LFT calculations of irregular function, namely $\frac{g^{(\mathrm{LFT})}_{\epsilon\ell m}(\mathbf{r})}{r}$. Panels (a)–(d) depict the cases of $\ell = 1$, 2, 3, and 6, respectively. For all the LFT calculations the total number of n_1 states is $n_1^{(\mathrm{tot})} = 25$ which corresponds to $\beta_{n_1} < 1$.

initio numerical solution of the inhomogeneous Schrödinger equation which employ a velocity mapping technique and which do not make use of the LFT approximation.

More specifically, this method uses a discretization of the Schrödinger equation on a grid of points in the radial coordinate r and an orbital angular momentum grid in ℓ. The main framework of the method is described in detail in Sec. 2.1 of Ref. [42] and below only three slight differences are highlighted. In order to represent a cw laser, the source term was changed to $S_0(\vec{r},t) = [1 + \mathrm{erf}(t/t_w)]z\psi_{\mathrm{init}}(\vec{r})$ with ψ_{init} either the $3p,m=0$ or $3p,m=1$ state. The time dependence, $1 + \mathrm{erf}(t/t_w)$, gives a smooth turn-on for the laser with time width of t_w; t_w is chosen to be of the order of a few picoseconds. The second difference is that the Schrödinger equation is solved until the transients from the laser turn on decayed to zero. The last difference was in how the differential cross section is extracted. The radial distribution in space slowly evolves with increasing distance from the atoms and the calculations become challenging as the region represented by the wave function increases. To achieve convergence in a smaller spatial region, the velocity distribution in the ρ direction is directly obtained. The wave function in r,ℓ is numerically summed over the orbital angular momenta ℓ yielding $\psi_m(\rho,z)$, where m is the azimuthal angular momentum. Finally, using standard numerical techniques a Hankel transformation is performed on the wave function $\psi_m(\rho,z)$ which reads

$$\psi_m(k_\rho,z) = \int d\rho\ \rho\ J_m(k_\rho\rho)\psi_m(\rho,z), \tag{45}$$

which can be related to the differential cross section. The cross section is proportional to $k_\rho|\psi_m(k_\rho,z)|^2$ in the limit that $z \to -\infty$. The k_ρ is related to the ρ in Fig. 6 through a scaling factor. The convergence of our results is tested with respect to number of angular momenta, number of radial grid points, time step, $|z|_{\max}$, t_w, and final time. The bandwidth that the following calculations exhibit is equal to 0.17 cm^{-1}. In addition, in order to check the validity of our velocity mapping calculation we directly compute numerically the differential cross section through the electron flux defined in Eq. (31). An agreement of the order of percent is observed solidifying our investigations.

One sees immediately in panels (a)–(d) of Fig. 6 that the LFT calculations are in good agreement with the full numerical

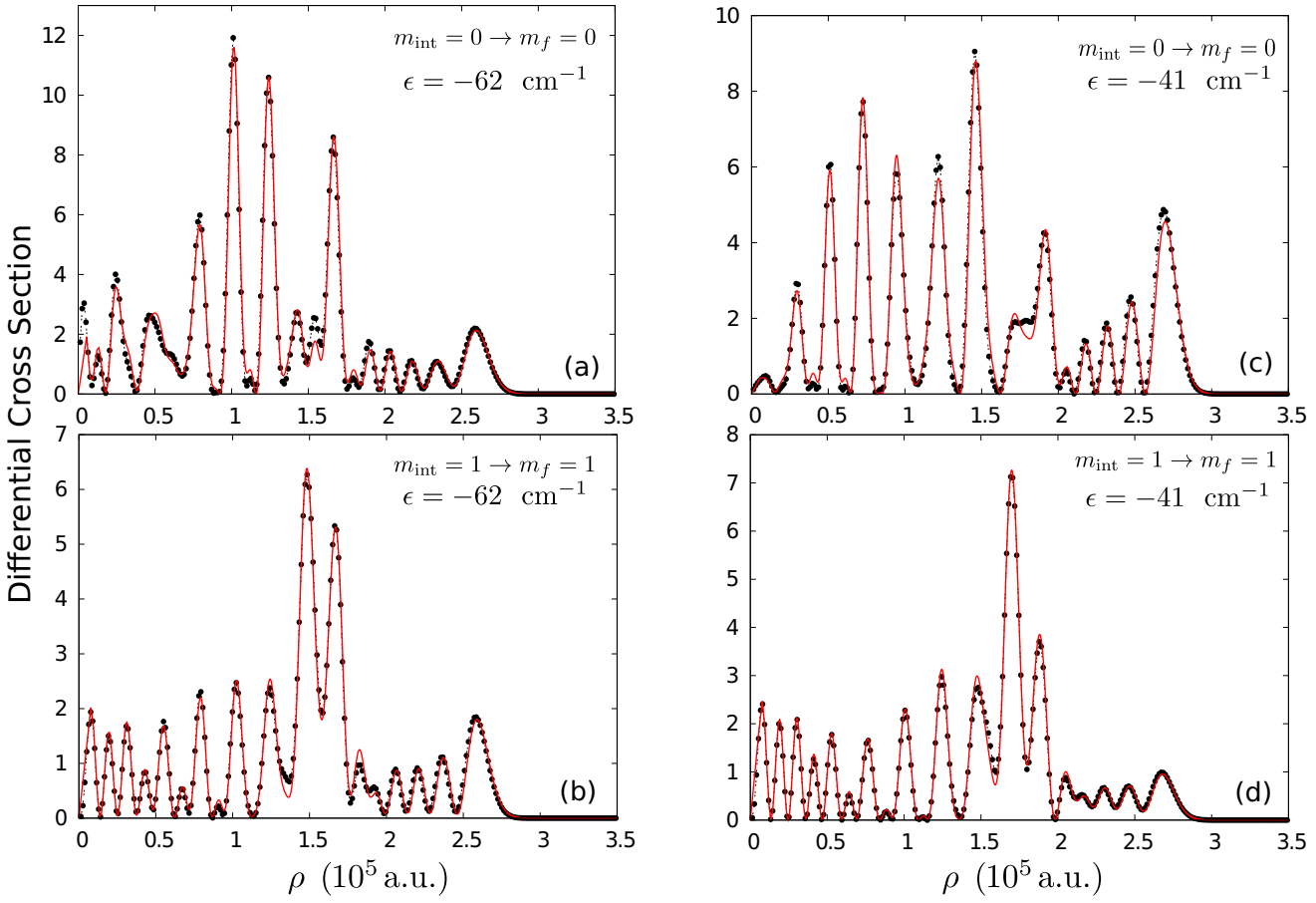

FIG. 6. (Color online) Differential cross section (in arbitrary units) for Na atoms as a function of the cylindrical coordinate ρ. The red solid lines indicate the LFT theory calculations, whereas the black dots denote the velocity mapping results from a direct solution of the two-dimensional inhomogeneous Schrödinger equation. Panels (a) and (b) refer to energy $\epsilon = -62\,\text{cm}^{-1}$ for the transitions $m_{\rm int} = 0 \to m_f = 0$ and $m_{\rm int} = 1 \to m_f = 1$, respectively. Similarly, panels (c) and (d) refer to energy $\epsilon = -41\ \text{cm}^{-1}$ for the transitions $m_{\rm int} = 0 \to m_f = 0$ and $m_{\rm int} = 1 \to m_f = 1$, respectively. In all cases the field strength is $F = 3590$ V/cm and the detector is placed at $z_{\rm det} = -1$ mm.

ones, with only minor areas of disagreement. In particular, the interference patterns in all calculations are essentially identical. An important point is that the observed discrepancies in the frame-transformed irregular functions for orbital angular momenta $\ell > 1$ do not exhibit any qualitative inaccuracies in the differential cross-section calculations. As was mentioned before this is due to the fact that the higher ℓ states are associated with negligible quantum defects for the case of alkali-metal atoms yielding minor contributions in the cross section.

VI. SUMMARY AND CONCLUSIONS

The present study reviews Harmin's Stark-effect theory and develops a standardized form of the corresponding LFT theory. In addition, the LFT Stark-effect theory is formulated in the traditional framework of scattering theory including its connections to the photoionization observables involving the dipole matrix elements, in particular the differential cross section. In order to quantitatively test the LFT, the present formulation does not use semiclassical WKB theory as was utilized by Harmin. Indeed, as was shown in Refs. [15,43] the WKB approximation yields discrepancies in the photoabsorption spectra within the LFT framework. However, the accuracy of the LFT treatment is improved by evaluating numerically the wave functions in the down-field degree of freedom [15]. Therefore, here the corresponding one-dimensional differential equations are solved within an eigenchannel R-matrix framework. This study has thoroughly investigated the core idea of the LFT theory, which in a nutshell defines a mapping between the irregular solutions of two regions, namely spherical solutions in the field-free region close to the origin and the parabolic coordinate solutions relevant from the core region all the way out to asymptotic distances. For positive energies, our calculations demonstrate that indeed the mapping formula Eq. (16) predicts the correct Coulomb irregular solution in spherical coordinates (see Figs. 3 and 4). On the other hand, at negative energies it is demonstrated (see Fig. 5) that the summation over solely down field states $\beta_{n_1} < 1$ imposes minor limitations in the accuracy of LFT calculation mainly for $\ell > 3$. We conjecture that this particular feature might provide additional insight into the origin of the differences between the numerical LFT and R-matrix treatment which were demonstrated in Ref. [15]. However, the investigation of this point goes beyond the scope of this study. On the other hand, our study investigates the concept of wave-function microscopy through calculations of

photoionization differential cross sections for a Na atom in the presence of a uniform electric field. The photoionization process studied is a resonant two-photon process where the laser field is assumed to be π polarized. The excellent agreement between the LFT and the full velocity mapping calculation has been conclusively demonstrated.

These findings suggest that the LFT theory passes the stringent tests of wave-function microscopy, and can be relied upon both to provide powerful physical insight and quantitatively accurate observables, even for a complicated observable such as the differential photoionization cross section in the atomic Stark effect.

ACKNOWLEDGMENTS

The authors acknowledge Ilya Fabrikant and Jesus Perez-Rios for helpful discussions. This work was supported by the US Department of Energy, Office of Science, Basic Energy Sciences, under Grants No. DE-SC0010545 (for P.G. and C.H.G.) and No. DE-SC0012193 (for F.R.).

APPENDIX: COULOMB FUNCTIONS FOR NONPOSITIVE HALF-INTEGER ANGULAR MOMENTUM AT NEGATIVE ENERGIES

In this Appendix we will present the regular and irregular Coulomb functions with nonpositive half-integer, either positive or negative, quantum numbers. The necessity for this particular type of solutions arises from the fact that they constitute the boundary conditions for the R-matrix eigenchannel calculations in the down field η degree of freedom at sufficient small distances where essentially the field term can be neglected. This corresponds in the field free case where the orbital angular momentum does not possess non-negative integer values.

The Schrödinger equation in the field free case for the η parabolic coordinate has the following form:

$$\frac{d^2}{d\eta^2} f^{\epsilon}_{\beta m}(\eta) + \left(\frac{\epsilon}{2} + \frac{1-m^2}{4\eta^2} + \frac{1-\beta}{\eta}\right) f^{\epsilon}_{\beta m}(\eta) = 0, \quad \text{(A1)}$$

where the energy ϵ is considered to be negative. Assuming that $\bar{\epsilon} = 2\epsilon/(1-\beta)^2$, $\zeta = \frac{1-\beta}{2}\eta$, and $\lambda = (m-1)/2$, Eq. (A1) can be transformed into the following differential equation:

$$\frac{d^2}{d\zeta^2} f^{\bar{\epsilon}}_{\lambda}(\zeta) + \left(\bar{\epsilon} - \frac{\lambda(\lambda+1)}{\zeta^2} + \frac{2}{\zeta}\right) f^{\bar{\epsilon}}_{\lambda}(\zeta) = 0, \quad \text{(A2)}$$

which for integer λ has two linearly independent energy normalized solutions whose relative phase is $\pi/2$ at small distances and negative energies

$$f^{\bar{\epsilon}}_{\lambda}(\zeta) = A(\bar{\nu},\lambda)^{1/2} S^{\bar{\epsilon}}_{\lambda}(\zeta), \quad \text{(A3)}$$

$$g^{\bar{\epsilon}}_{\lambda}(\zeta) = A(\bar{\nu},\lambda)^{1/2} S^{\bar{\epsilon}}_{\lambda}(\zeta)\cot[(2\lambda+1)\pi] - \frac{A(\bar{\nu},\lambda)^{-1/2} S^{\bar{\epsilon}}_{-\lambda-1}(\zeta)}{\sin[(2\lambda+1)\pi]}, \quad \text{(A4)}$$

where $\bar{\nu} = 1/\sqrt{-\bar{\epsilon}}$, $A(\bar{\nu},\lambda) = \frac{\Gamma(\lambda+\bar{\nu}+1)}{\bar{\nu}^{2\lambda+1}\Gamma(\bar{\nu}-\lambda)}$, and the function $S^{\bar{\epsilon}}_{\lambda}(\zeta)$ is obtained by the following relation:

$$S^{\bar{\epsilon}}_{\lambda}(\zeta) = 2^{\lambda+1/2}\zeta^{\lambda+1}e^{-\zeta/\bar{\nu}}\ {}_1\bar{F}_1(\lambda-\bar{\nu}+1; 2+2\lambda; 2\zeta/\bar{\nu}), \quad \text{(A5)}$$

where the function ${}_1\bar{F}_1$ denotes the regularized hypergeometric function ${}_1F_1$. One basic property of this function is that it remains finite even when its second argument is a nonpositive integer. We recall that the hypergeometric ${}_1F_1(a;b;x)$ diverges when $b = -1, -2, -3, \ldots$.

Moreover, we observe that when λ acquires half-integer values, i.e., $\lambda = \lambda_c$, the nominator and denominator of $g^{\bar{\epsilon}}_{\lambda}$ in Eq. (A4) both vanish. Therefore, employing the l'Hospital's theorem on $g^{\bar{\epsilon}}_{\lambda}$ in Eq. (A4) we obtain the following expression:

$$\bar{g}^{\bar{\epsilon}}_{\lambda_c}(\zeta) = \frac{1}{2\pi}\frac{\partial f^{\bar{\epsilon}}_{\lambda}(\zeta)}{\partial\lambda}\bigg|_{\lambda=\lambda_c} - \frac{1}{2\pi\cos[(2\lambda_c+1)\pi]}\frac{\partial f^{\bar{\epsilon}}_{-\lambda-1}(\zeta)}{\partial\lambda}\bigg|_{\lambda=\lambda_c}. \quad \text{(A6)}$$

Hence Eqs. (A3) and (A6) correspond to the regular and irregular Coulomb functions for nonpositive half-integers at negative energies, respectively. This particular set of solutions possess $\pi/2$-relative phase at short distances and they used as boundary conditions in the eigenchannel R-matrix calculations. A similar construction is possible with the help of Ref. [44] for positive energies but it is straightforward and not presented here.

[1] U. Fano, Phys. Rev. A **24**, 619 (1981).
[2] D. A. Harmin, Phys. Rev. A **26**, 2656 (1982).
[3] D. A. Harmin, Phys. Rev. Lett. **49**, 128 (1982).
[4] D. A. Harmin, Phys. Rev. A **24**, 2491 (1981).
[5] C. H. Greene, Phys. Rev. A **36**, 4236 (1987).
[6] H. Y. Wong, A. R. P. Rau, and C. H. Greene, Phys. Rev. A **37**, 2393 (1988).
[7] A. R. P. Rau and H. Y. Wong, Phys. Rev. A **37**, 632 (1988).
[8] C. H. Greene and N. Rouze, Z. Phys. D **9**, 219 (1988).
[9] V. Z. Slonim and C. H. Greene, Radiat. Effects Defects Solids **122**, 679 (1991).
[10] B. E. Granger and D. Blume, Phys. Rev. Lett **92**, 133202 (2004).
[11] P. Giannakeas, F. K. Diakonos, and P. Schmelcher, Phys. Rev. A **86**, 042703 (2012).
[12] B. Heß, P. Giannakeas, and P. Schmelcher, Phys. Rev. A **89**, 052716 (2014).
[13] C. Zhang and C. H. Greene, Phys. Rev. A **88**, 012715 (2013).
[14] P. Giannakeas, V. S. Melezhik, and P. Schmelcher, Phys. Rev. Lett. **111**, 183201 (2013).
[15] G. D. Stevens, C.-H. Iu, T. Bergeman, H. J. Metcalf, I. Seipp, K. T. Taylor, and D. Delande, Phys. Rev. A **53**, 1349 (1996).
[16] S. Cohen, M. M. Harb, A. Ollagnier, F. Robicheaux, M. J. J. Vrakking, T. Barillot, F. Lépine, and C. Bordas, Phys. Rev. Lett. **110**, 183001 (2013).

[17] J. Itatani, J. Levesque, D. Zeidler, H. Niikura, H. Pépin, J.-C. Kieffer, P. B. Corkum, and D. M. Villeneuve, Nature (London) **432**, 867 (2004).
[18] C. Bordas, F. Lépine, C. Nicole, and M. J. J. Vrakking, Phys. Rev. A **68**, 012709 (2003).
[19] C. Nicole, H. L. Offerhaus, M. J. J. Vrakking, F. Lépine, and C. Bordas, Phys. Rev. Lett. **88**, 133001 (2002).
[20] V. D. Kondratovich and V. N. Ostrovsky, J. Phys. B: At. Mol. Phys. **17**, 1981 (1984).
[21] V. D. Kondratovich and V. N. Ostrovsky, J. Phys. B: At. Mol. Phys. **17**, 2011 (1984).
[22] V. D. Kondratovich and V. N. Ostrovsky, J. Phys. B: At., Mol. Opt. Phys. **23**, 21 (1990).
[23] V. D. Kondratovich and V. N. Ostrovsky, J. Phys. B: At., Mol. Opt. Phys. **23**, 3785 (1990).
[24] D. J. Armstrong, C. H. Greene, R. P. Wood, and J. Cooper, Phys. Rev. Lett. **70**, 2379 (1993).
[25] D. J. Armstrong and C. H. Greene, Phys. Rev. A **50**, 4956 (1994).
[26] F. Robicheaux, C. Wesdorp, and L. D. Noordam, Phys. Rev. A **60**, 1420 (1999).
[27] C. Blondel, C. Delsart, and F. Dulieu, Phys. Rev. Lett. **77**, 3755 (1996).
[28] F. Texier, Phys. Rev. A **71**, 013403 (2005).
[29] L. B. Zhao, I. I. Fabrikant, M. L. Du, and C. Bordas, Phys. Rev. A **86**, 053413 (2012).
[30] For further details, see P. Giannakeas, F. Robicheaux, and C. H. Greene (unpublished).
[31] L. S. Rodberg and R. M. Thaler, *Introduction to the Quantum Theory of Scattering*, Pure and Applied Physics, A Series of Monographs and Textbooks, Vol. 26 (Academic Press, New York, 1970).
[32] E. N. Economou, *Green's Functions in Quantum Physics*, 3rd ed., Springer Series in Solid-State Sciences (Springer, New York, 2006).
[33] C. H. Greene, U. Fano, and G. Strinati, Phys. Rev. A **19**, 1485 (1979).
[34] F. Robicheaux and J. Shaw, Phys. Rev. A **56**, 278 (1997).
[35] L. B. Zhao, I. I. Fabrikant, J. B. Delos, F. Lépine, S. Cohen, and C. Bordas, Phys. Rev. A **85**, 053421 (2012).
[36] C. H. Greene, Phys. Rev. A **28**, 2209 (1983).
[37] C. H. Greene and L. Kim, Phys. Rev. A **38**, 5953 (1988).
[38] M. Aymar, C. H. Greene, and E. Luc-Koenig, Rev. Mod. Phys. **68**, 1015 (1996).
[39] P. Descouvemont and D. Baye, Rep. Prog. Phys. **73**, 036301 (2010).
[40] U. Fano and C. M. Lee, Phys. Rev. Lett. **31**, 1573 (1973).
[41] C. De Boor, J. Approx. Theory **6**, 50 (1972).
[42] T. Topçu and F. Robicheaux, J. Phys. B: At., Mol. Opt. Phys. **40**, 1925 (2007).
[43] M. Grütter, O. Zehnder, T. P. Softley, and F. Merkt, J. Phys. B: At., Mol. Opt. Phys. **41**, 115001 (2008).
[44] F. W. Olver, *NIST Handbook of Mathematical Functions* (Cambridge University Press, Cambridge, UK, 2010).